



# Öpik-type collision probability for high-inclination orbits: Targets on eccentric orbits



Petr Pokorný\*, David Vokrouhlický

*Institute of Astronomy, Charles University, V Holešovičkách 2, CZ-18000, Prague 8, Czech Republic*

## ARTICLE INFO

### Article history:

Received 22 April 2013

Revised 13 June 2013

Accepted 14 June 2013

Available online 28 June 2013

### Keywords:

Celestial mechanics

Impact processes

Asteroids

Interplanetary dust

## ABSTRACT

Traditional evaluation of collision probability between two bodies on bound heliocentric or planetocentric orbits include assumptions that are often only an approximation of their real motion. In particular, these approaches require (i) the orbital eccentricity and inclination of both target and projectile long-term constant, and (ii) their longitude of ascending node and argument of pericenter precessing uniformly in time. Both conditions (i) and (ii) are satisfied for orbits with very small eccentricities and inclinations only. When either of these two elements is large, a tidal perturbation by planets, or the Sun in a planetocentric configuration, makes these elements oscillate in a correlation with the non-linear evolution of the secular angles. Vokrouhlický et al. (Vokrouhlický, D., Pokorný, P., Nesvorný, D. [2012]. *Icarus* 219, 150–160) developed an approach which allows the orbit of the projectile undergo such a general secular evolution. An assumption of the circular orbit of the target, however, was a significant drawback of their method. Here, we extend Vokrouhlický et al.'s work to allow a general eccentric and precessing orbit of the target (assuming though fixed orbital plane in space). We test predictions of our new approach, as well as previous theories, against a direct numerical integration and estimate their validity. A particular run is performed for E-belt projectiles impacting terrestrial planets. We conclude a surprisingly good correspondence of the directly obtained impact record from the numerical simulation and the estimate from our theory. Based on these results, we infer that the crater density from E-belt projectiles on Mercury should be roughly comparable (or only slightly larger) to that on our Moon.

© 2013 Elsevier Inc. All rights reserved.

## 1. Introduction

Planets, accompanied with their satellites, are not alone to revolve about the Sun. There is a myriad of smaller bodies, ranging from asteroids and comets down to sizes of dust particles, orbiting the Sun. Some of them may occasionally share the same region in space where planets move, and thus could impact on them. Living in large populations, these smaller bodies may also hit each other. Evaluating the small, though non-zero, probability of these events is often an important information in planetary studies. In this work, we do not deal with an impact probability of a specific projectile over a short timescale. Rather, we have in mind an evaluation of a mean impact probability averaged over a timescale equal or longer than that characterizing a secular evolution of the projectile orbit.

Öpik (1951) was the first to deal with this problem in the modern astronomical literature. This work assumed a target on a circular orbit fixed in space, sweeping through a population of projectiles on bound heliocentric orbits with constant eccentricities and

inclinations. Öpik's theory was later generalized for targets on eccentric and inclined orbits by Wetherill (1967) and Greenberg (1982) which themselves undergo a simple secular evolution, again keeping the assumption of a long-term constant values of orbital eccentricity and inclination. A slightly different approach was independently proposed by Kessler (1981).

All these above mentioned approaches are frequently used to determine a collision probability among members of a population of small bodies or with respect to planets and their satellites. For instance, all collisional evolution codes are based on either Wetherill's or Greenberg's variants of the method, some occasionally use the Kessler's approach. All these standard theories assume the orbital eccentricity  $e$  and inclination  $i$  during the secular evolution of target and projectiles are constant. This assumption is not exactly correct even for moderate values of  $e$  and  $i$ . Still, the variations of  $e$  and  $i$  are mostly small enough such that the population average, and often other unknown parameters in the model, make the results grossly justified. However, when either of the projectile or the target orbits have high inclination and/or high eccentricity, application of the traditional collision model is questionable. This is because variations of  $e$  and  $i$  during the secular cycle may be large, and the secular angles such as the longitude of node and pericenter may exhibit a strongly non-linear evolution with time.

\* Corresponding author.

E-mail addresses: [petr.pokorny@volny.cz](mailto:petr.pokorny@volny.cz) (P. Pokorný), [vokrouhli@cesnet.cz](mailto:vokrouhli@cesnet.cz) (D. Vokrouhlický).

About half a century ago elements of these dynamical phenomena were introduced by Lidov (1961, 1962) in space geodesy and independently by Kozai (1962) in planetary astronomy. Later, more complex theories, allowing for instance a planet crossing, were developed. These results were needed, because certain populations of small bodies reside on such orbits and thus undergo the corresponding orbital evolution: all classes of comets and their related meteoroid streams, meteoroids in the sporadic complex, etc. As a result, the traditional collision probability methods may provide disputable results when evaluating their impact chances with the Earth, for instance.

This situation motivated Vokrouhlický et al. (2012) to formulate a generalized Öpik-type collision probability theory. In their model the projectile orbit was allowed to undergo Lidov–Kozai oscillations, and with a simple generalization even more complex, secular evolution. However, a persisting drawback was the assumption of a circular and fixed orbit of the target. Here we extend this earlier work and allow the target orbit be eccentric and uniformly precessing in space. While not so critical for Earth or Venus, this generalization makes our approach quite more suitable for evaluation of impact probability on Mercury or Mars, as examples.

Mathematical preliminaries are introduced in Section 2.1. Section 2.2 is a brief summary of the Lidov–Kozai dynamics, and the core formulation of our collision probability model is given in Sections 2.3 and 2.4. In Section 3 we provide simple-configuration runs which illustrate our main results and help justify our numerical approach. Finally, Section 4 contains simulation motivated by recent work of Bottke et al. (2012): projectiles originating in today’s extinct extension of the main asteroid belt, known as the E-belt, are propagated in the gravity field of the Sun and all planets. We record direct impacts onto terrestrial planets as provided by our numerical simulation and compare them with an estimation from our theory. An emphasis is given to impacts on Mercury which was not included in Bottke et al. (2012).

## 2. Theory

### 2.1. Reference frames and notation

In this section we introduce necessary mathematical concepts and notation used throughout the paper. Obviously, both closely follow the work of Vokrouhlický et al. (2012), allowing now an eccentric orbit of the target.

We start with a description of the projectile orbit near the nodal crossings of the target plane (for sake of definiteness we assume both are on heliocentric orbits). Assume the projectile resides on a general elliptic orbit described with osculating Keplerian elements: the semimajor axis  $a$ , the eccentricity  $e$ , the inclination  $i$ , the longitude of node  $\Omega$ , the argument of pericenter  $\omega$  and the true anomaly  $f$ . The angular parameters  $i$ ,  $\Omega$  and  $\omega$  are defined with respect to the inertial frame  $(X, Y, Z)$ , whose reference plane  $(X, Y)$  coincides with that of the target’s fixed orbital plane about the Sun.<sup>1</sup> The projectile orbit intersects the  $(X, Y)$  reference plane at the ascending node, where  $f = f_n = -\omega$ , and the descending node, where  $f = f_n = \pi - \omega$ . The description of the orbit near the nodal intersections benefits from introduction of the reference basis  $(\mathbf{e}_r, \mathbf{e}_\phi, \mathbf{e}_z)$  composed of the three orthonormal vectors with the origin at the ascending or descending nodes. The vectors  $\mathbf{e}_r$  and  $\mathbf{e}_\phi$  point to the radial and longitude directions at the respective node, and the vector  $\mathbf{e}_z$  along the  $Z$  axis of the inertial frame. Thus in our definition, the radial and longitude directions, i.e.  $\mathbf{e}_r$  and  $\mathbf{e}_\phi$  vectors, at the descend-

ing node are opposite to their values at the ascending node.

The heliocentric position vector  $\mathbf{r}$  describing the elliptic orbit of the projectile generally reads

$$\mathbf{r}(f) = r(f)[\mathbf{a} \cos(\omega + f) + \mathbf{b} \sin(\omega + f)], \quad (1)$$

with  $r(f) = a\eta^2/(1 + e \cos f)$  and  $\eta = \sqrt{1 - e^2}$ . The unit vector  $\mathbf{a}^T = (\cos \Omega, \sin \Omega, 0)$  is directed along the ascending node, and  $\mathbf{b}^T = (-\cos i \sin \Omega, \cos i \cos \Omega, \sin i)$  is in the orbital plane, normal to  $\mathbf{a}$ . As a result, at the ascending node we have  $\mathbf{a} = \mathbf{e}_r$  and  $\mathbf{b} = \cos i \mathbf{e}_\phi + \sin i \mathbf{e}_z$ , while at the descending node we have  $\mathbf{a} = -\mathbf{e}_r$  and  $\mathbf{b} = -\cos i \mathbf{e}_\phi + \sin i \mathbf{e}_z$ . Now expand  $\mathbf{r}(f)$  near the ascending and descending nodes, where the heliocentric distance is  $r = a\eta^2/(1 \pm e \cos \omega)$  respectively (the upper sign for the ascending node). Introducing an infinitesimal increment  $df$  of the true anomaly,  $f = f_n + df$ , we obtain  $\mathbf{r}(f) = r \mathbf{e}_r + d\mathbf{r}$ , with

$$d\mathbf{r} = r \mathbf{A}_1 df + \frac{r}{2} \mathbf{A}_2 df^2 + \mathcal{O}(df^3). \quad (2)$$

Eq. (2) helps to locally describe the elliptic orbit of the projectile with  $df = 0$  at the respective node. The first term is the crudest rectilinear approximation, while the second term describes the local curvature of the elliptic orbit. The first- and second-order vectorial coefficients read (the upper sign for the ascending node intersection and the lower sign for the descending node intersection)

$$\mathbf{A}_1 = \mp \frac{e \sin \omega}{P} \mathbf{e}_r + (\cos i \mathbf{e}_\phi \pm \sin i \mathbf{e}_z), \quad (3)$$

$$\begin{aligned} \mathbf{A}_2 = & -2 \left[ 1 - \frac{3}{2P} + \frac{\eta^2}{P^2} \right] \mathbf{e}_r \\ & - 2 \frac{e \sin \omega}{P} (\pm \cos i \mathbf{e}_\phi + \sin i \mathbf{e}_z), \end{aligned} \quad (4)$$

where  $P = a\eta^2/r$ .

Next, we use a similar framework to describe motion of the target body. The target body is assumed to move on an elliptic heliocentric orbit with the semimajor axis  $a_0$ , the eccentricity  $e_0$  and the argument of pericenter  $\omega_0$  in the  $(X, Y)$  reference plane. Without loss of generality we set  $\omega_0 = 0$  in our coordinate system. Choosing a certain value  $f_0$  of the true anomaly, the position vector  $\mathbf{r}_0$  of the target can again be described as  $\mathbf{r}_0(f) = r_0 \mathbf{e}_r + d\mathbf{r}_0$  in its orbital vicinity<sup>2</sup>  $f = f_0 + df$  ( $r_0$  is the target’s heliocentric distance for  $f = f_0$ ). We now have

$$d\mathbf{r}_0 = r_0 \mathbf{A}_{10} df + \frac{r_0}{2} \mathbf{A}_{20} df^2 + \mathcal{O}(df^3), \quad (5)$$

with

$$\mathbf{A}_{10} = \frac{e_0 \sin f_0}{P_0} \mathbf{e}_r + \mathbf{e}_\phi, \quad (6)$$

$$\mathbf{A}_{20} = -2 \left[ 1 - \frac{3}{2P_0} + \frac{\eta_0^2}{P_0^2} \right] \mathbf{e}_r \pm 2 \frac{e_0 \sin f_0}{P} \mathbf{e}_\phi, \quad (7)$$

where  $P_0 = a_0 \eta_0^2 / r_0$  and  $\eta_0 = \sqrt{1 - e_0^2}$ . For further use we shall express coefficients in  $\mathbf{A}_{10}$  and  $\mathbf{A}_{20}$  as a function of  $r_0$  rather than  $f_0$ . To that goal we have a relation  $e_0 \sin f_0 = \eta_0 R_\pm$  with  $R_\pm = \pm \sqrt{(r_0 - r_1)(r_2 - r_0)} / r_0$ , where  $r_1 = a_0(1 - e_0)$  and  $r_2 = a_0(1 + e_0)$  stand for the perihelion and aphelion distances of the target orbit respectively. The upper and lower sign in  $R_\pm$  correspond to  $f_0$  values in the interval  $(0, \pi)$  and  $(\pi, 2\pi)$  respectively, and need to be considered separately.

Previous notation also helps us to express the orbital velocity  $\mathbf{v}$  of the projectile at the nodal intersection and the orbital velocity  $\mathbf{v}_0$  of the target body. Using arbitrarily  $V_0 = n_0 a_0$  as a velocity normalization ( $n_0$  is the mean motion of the target), we use the linear term

<sup>1</sup> We assume  $i \neq 0$ , otherwise a non-singular set of orbital elements would be needed. As in Vokrouhlický et al. (2012) we keep a close similarity in notation to the works of Öpik (1951) and Wetherill (1967) and thus we only consider a non-planar case.

<sup>2</sup> The unit vectors  $\mathbf{e}_r$  and  $\mathbf{e}_\phi$  are assumed at the point of the orbit with  $f = f_0$ .

in Eq. (2) and differentiation by time to obtain

$$\begin{aligned} \mathbf{v} &= V_0 \sqrt{\frac{a_0}{r}} \sqrt{P} \mathbf{A}_1 \\ &= V_0 \sqrt{\frac{a_0}{r}} \sqrt{P} \left[ \mp \frac{e \sin \omega}{P} \mathbf{e}_r + (\cos i \mathbf{e}_\phi \pm \sin i \mathbf{e}_z) \right], \end{aligned} \quad (8)$$

where again the upper and lower sign correspond to the ascending and descending nodes respectively. Similarly, for the target body we have

$$\mathbf{v}_0 = V_0 F \mathbf{A}_{10} = V_0 [R_\pm \mathbf{e}_r + F \mathbf{e}_\phi], \quad (9)$$

where  $F = \eta_0 a_0 / r_0$ .

Finally, the relative velocity  $\mathbf{V} = \mathbf{v} - \mathbf{v}_0$  of the projectile with respect to the target at the exact intersection condition

$$r_0 = r = \frac{a\eta^2}{1 \pm e \cos \omega} \quad (10)$$

can be obtained from Eqs. (8) and (9). For further convenience we shall express  $\mathbf{V}$  in a local frame of rotated vectors  $(\mathbf{e}_a, \mathbf{e}_b, \mathbf{e}_z)$ , where  $\mathbf{e}_a$  is directed to the local apex of target's motion,  $\mathbf{e}_b = \mathbf{e}_a \times \mathbf{e}_z$  and  $\mathbf{e}_z$  always along the  $Z$  axis of the inertial frame. Henceforth

$$\mathbf{e}_a = \frac{R_\pm \mathbf{e}_r + F \mathbf{e}_\phi}{\sqrt{R_\pm^2 + F^2}}, \quad (11)$$

$$\mathbf{e}_b = \frac{F \mathbf{e}_r - R_\pm \mathbf{e}_\phi}{\sqrt{R_\pm^2 + F^2}}, \quad (12)$$

with also  $R_\pm^2 + F^2 = 2(a_0/r_0) - 1$ . Thus the corresponding velocity components  $V_a = \mathbf{V} \cdot \mathbf{e}_a$ ,  $V_b = \mathbf{V} \cdot \mathbf{e}_b$  and  $V_z = \mathbf{V} \cdot \mathbf{e}_z$  read

$$V_a = \frac{V_0}{\sqrt{R_\pm^2 + F^2}} \left[ \sqrt{\frac{a_0}{r}} \sqrt{P} \left( \mp R_\pm \frac{e \sin \omega}{P} + F \cos i \right) - (R_\pm^2 + F^2) \right], \quad (13)$$

$$V_b = \frac{V_0}{\sqrt{R_\pm^2 + F^2}} \sqrt{\frac{a_0}{r}} \sqrt{P} \left( \mp F \frac{e \sin \omega}{P} - R_\pm \cos i \right), \quad (14)$$

$$V_z = \pm V_0 \sqrt{\frac{a_0}{r}} \sqrt{P} \sin i. \quad (15)$$

## 2.2. Secular evolution in the Lidov–Kozai model

As mentioned in Section 1, we shall use the Lidov–Kozai model for the secular evolution of the projectile orbit. We shall only briefly recall fundamental facts of this model studied thoroughly in literature (e.g., Lidov, 1961, 1962; Kozai, 1962; Morbidelli, 2002).

We assume a single perturber (such as Jupiter in studies of motion of small bodies in the inner Solar System) on a circular orbit, coplanar with the target. The target is assumed massless, such that it leaves the orbit of perturber fixed. Vice versa, the perturber makes the eccentric orbit of the target uniformly precess in their common orbital plane.

The effect of the perturber on the projectile's orbit are more spectacular. A simple, first-order secular perturbation model, prohibiting mean-motion resonances with the perturber, is obtained by double averaging of the averaged perturbing function over the mean longitude of the perturber and the projectile heliocentric motions (Morbidelli, 2002). Eliminated orbital elements and symmetries of the problem provide three integrals of motion: (i) the semimajor axis  $a$  of the projectile heliocentric orbit, (ii) the projection of the projectile's orbital angular momentum on the  $Z$  axis, and (iii) the value of the perturbing function  $\mathcal{P}$ . The second integral

(ii) implies  $c = \sqrt{1 - e^2} \cos i = \text{const.}$ , which conveniently helps to eliminate either of the two elements, eccentricity  $e$  or inclination  $i$ , for the latter and a conserved quantity  $c$ . The situation with the third integral (iii) is more complicated because its efficient evaluation may need numerical methods. This is especially true if the projectile's orbit crosses that of the perturber (e.g., Bailey et al., 1992; Thomas and Morbidelli, 1996; Gronchi and Milani, 1998, 1999; Morbidelli, 2002). While our method might be applied in these situations as well, most work would need to be performed numerically. We rather opt for a semi-numerical approach in spite of crude approximations in developing  $\mathcal{P}$ . In particular, of the multipole series representation used by Kozai (1962) we keep only the lowest-order quadrupole term. Generalizations to higher-order terms are straightforward at the expense of some algebraic effort. In our approximation (iii) above implies first integral (e.g., Kozai, 1962; Kinoshita and Nakai, 2007)

$$\frac{1}{\eta^2} [(2 + 3e^2)(3c^2 - \eta^2) + 15(\eta^2 - c^2)(k^2 - h^2)] = C, \quad (16)$$

where  $k = e \cos \omega$  and  $h = e \sin \omega$ . The topology of  $C$ -isolines in the  $(k, h)$  space was extensively studied and does not need to be reminded in detail. When  $|c|$  is very close to unity the level curves of constant  $C$  are very close to circles about the origin of  $(k, h)$  plane. In this limit, the values of  $e$  and  $i$  are very small and they are well conserved very during the whole Kozai cycle, which is in an accordance with the assumptions of Opik's and Wetherill's collisional theories. Decreasing the value of  $|c|$  causes the level curves of constant  $C$  to transform from circles to ovals until reaching the critical value  $|c| = \sqrt{3/5}$ , where the topology adapts to a bifurcation of two different stationary solutions at the  $h$  axis (i.e.,  $k = e \cos \omega = 0$ ): (i) for  $C > 2(3c^2 - 1)$  the orbits circulate about the origin, but the variations may significantly increase the values  $e$  or  $i$  leading to very eccentric or inclined orbits, and (ii) for  $C < 2(3c^2 - 1)$  the orbits circulate about the stationary points on the  $h$  axis. For a given  $c$  value, the maximal values of  $e$  and  $\cos i$  are limited by  $\sqrt{1 - c^2}$  (for more rigorous specification of the intervals of  $e$  and  $i$  for given  $c$  and  $C$  see, for instance, Kinoshita and Nakai (2007), Eq. (31) and Eq. (32)).

## 2.3. Evaluating collision probability: target at a given heliocentric distance

In this Section we assume the target body at a given heliocentric distance  $r_0$  on its orbit and consider its collision probability with the projectile. We follow the Öpik–Wetherill method recalled in some detail by Vokrouhlický et al. (2012) (Section 3). In particular, the collision probability  $\Pi$  is composed of two independent parts: (i) the probability  $\Pi_1$  that during one cycle of secular evolution of the projectile's orbit its nodal crossing is sufficiently close to the target's orbit, and (ii) the probability  $\Pi_2$  that the target itself is close enough to the nodal crossing of the projectile's orbit. Since our assumptions about the target's orbit are identical to those in Wetherill, namely fixed eccentricity value  $e_0$  and uniformly precessing argument of pericenter  $\omega_0$ , we can use Wetherill (1967) result for  $\Pi_2$ . Put in our variables, notably using Eqs. (13)–(15), we obtain

$$\Pi_2 = \frac{\tau}{4a_0 \sqrt{R_\pm^2 + F^2}} \sqrt{\frac{V^2}{V^2 - V_a^2}}, \quad (17)$$

where  $V^2 = V_a^2 + V_b^2 + V_z^2$  is the relative velocity of the projectile and the target at the exact intersection of their orbits and  $\tau$  is the target's radius (we assume projectile negligibly small, otherwise  $\tau$  would have been a sum of target and projectile radii). Obviously,  $\Pi_2$  is to be evaluated at all possible nodal crossings of the projectile and target orbits (see below). The major modification of Wetherill's

approach consists now in an evaluation of  $\Pi_1$  (see also Vokrouhlický et al., 2012). This is because we consider a more complex secular evolution of the projectile's orbit.

Determination of  $\Pi_1$  is based on analysis of the orbit geometry near the nodal crossing. This is because the target (and potentially also the projectile) has a finite radius  $\tau$  and thus the impact occurs not only at the exact orbit crossing expressed by Eq. (10) which we rewrite as (upper and lower sign for the ascending and descending node crossings)

$$\alpha(1 \pm k) = \eta^2 \tag{18}$$

with  $\alpha = r_0/a$ . Eq. (18) yield circles with a displaced center in the  $(k, h)$  space. The orbit-intersection conditions now correspond to a crossing of these circles with the  $C = \text{const.}$  lines from Eq. (16) describing the secular evolution of the projectile's orbit. This simple quadrupole approximation of the Lidov–Kozai model yields up to eight such crossings (as compared to maximum of four crossings for two ellipses of fixed eccentricities, e.g. Fig. 1 in Wetherill (1967)).

Consider the local geometry of the target and projectile orbits near the node of the latter. Eqs. (2) and (5), in which we shall retain only linear terms, help us to describe the situation. The reference longitude in the  $(X, Y)$  plane at which we construct the radial  $\mathbf{e}_r$  and longitudinal  $\mathbf{e}_\phi$  vectors of the local reference frame  $(\mathbf{e}_r, \mathbf{e}_\phi, \mathbf{e}_z)$  is given by the chosen node of the projectile orbit. We, however, displace the origin of frame to the position of the target at the same

longitude. As a result the infinitesimal (rectilinear) arc of the target orbit is given by

$$\Delta \mathbf{r}_0(\lambda') = r_0 \mathbf{A}_{10} \lambda' + \mathcal{O}(\lambda'^2), \tag{19}$$

where  $r_0$  is the heliocentric distance of the origin and  $\lambda'$  parameterizes the orbit. Note that, unlike in Vokrouhlický et al. (2012),  $\mathbf{A}_{10}$  from Eq. (6) has now both longitudinal and radial components. This is due to eccentricity of the target's orbit. Similarly, the infinitesimal arc of the projectile's orbit reads

$$\Delta \mathbf{r}(\lambda) = (r - r_0) \mathbf{e}_r + r \mathbf{A}_1 \lambda + \mathcal{O}(\lambda^2), \tag{20}$$

in our reference system. Here  $r$  is the heliocentric distance of the node crossing. Because generally  $r \neq r_0$ , we have a radial displacement of the projectile's node expressed by the first term in Eq. (20). Parameter  $\lambda$  again serves to span different orbital locations of the projectile. The square of the projectile-target distance is simply  $d^2(\lambda, \lambda') = [\Delta \mathbf{r} - \Delta \mathbf{r}_0] \cdot [\Delta \mathbf{r} - \Delta \mathbf{r}_0]$ . We seek a minimum of  $d^2(\lambda, \lambda')$  on the  $(\lambda, \lambda')$  space, a task which leads to a simple system of two linear algebraic equations in our rectilinear approximation for both orbits. Solving them for  $\lambda$  and  $\lambda'$  we obtain the minimum orbital distance  $d_{\min}$

$$d_{\min} = \frac{(r - r_0) \sin i}{\sqrt{(1 + \beta^2) \sin^2 i + (\gamma - \beta \cos i)^2}}, \tag{21}$$

where  $\beta = r_0 R_{\pm} / (a_0 \eta_0)$  and  $\gamma = \mp e \sin \omega / P$ . Note  $d_{\min}$  is a function of assumed fixed  $r_0$  and orbital parameters of the projectile with the nodal distance  $r = a \eta^2 / (1 \pm e \cos \omega)$ . All possibilities with  $d_{\min} \leq \tau$

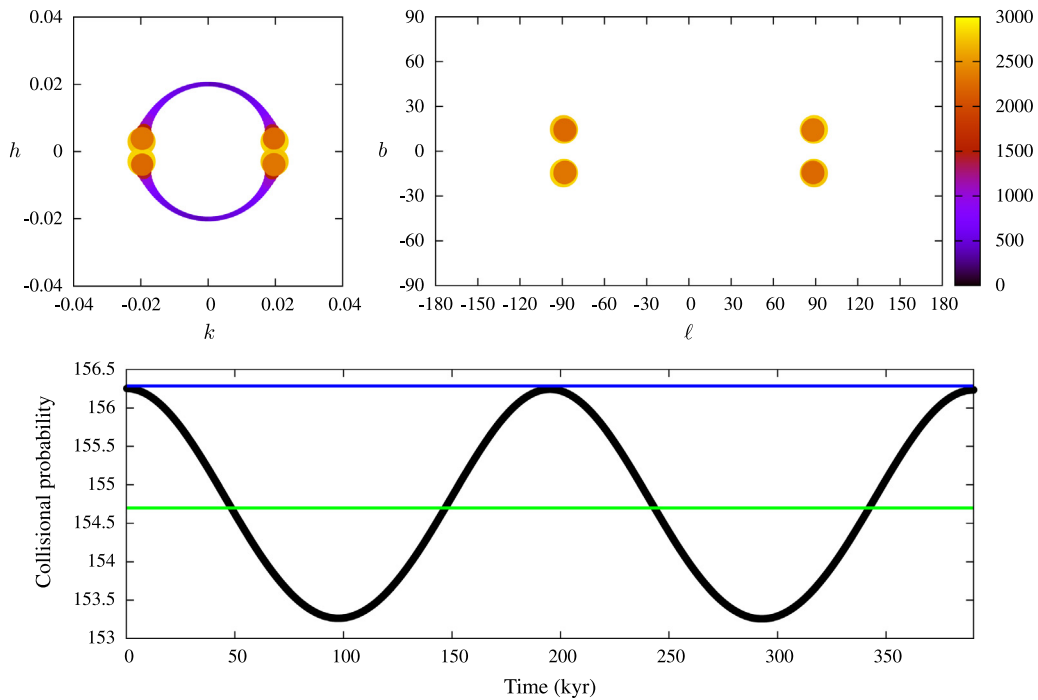


**Fig. 1.** Secular evolution, impact geometries (radiant position) and intrinsic impact probability. Massless target on Mercury-like orbit with the semimajor axis  $a_0 = 0.3871$  AU and the eccentricity  $e_0 = 0.2056$ . Projectile has the semimajor axis  $a = 0.4$  AU, and initial eccentricity  $e = 0.02$ , inclination  $i = 3^\circ$  and argument of pericenter  $\omega = 0^\circ$ . Single perturbing planet on a Jupiter-like orbit, coplanar with the target is assumed. Top and left: Secular evolution track of the projectile orbit is a small circle in the  $(k, h) = e(\cos \omega, \sin \omega)$  plane (black curve underneath the color-coded pattern). Because the orbit of target is eccentric, true impacts are possible along the whole trajectory characterizing the secular evolution of the projectile – suffice to independently tune the longitude of pericenter of the target. The intrinsic collision probability for that configuration is given by our function  $p(r_0)$  from Eq. (25). The color pattern with the color bar on the right gives  $p(r_0)$  in  $(\text{AU}^{-2} \text{y}^{-1})$ . The highly increased intrinsic collision probability for  $h \simeq 0$  values correspond to near pericentric impacts (see Appendix of Vokrouhlický et al., 2012). Top and right: Radiant positions of impact geometries as seen by observer at the target body; the abscissa is the longitude  $\ell$  measured from the apex direction, the ordinate is the latitude  $b$  (both in degrees). Even though there is an infinite number of impact configurations, the small eccentricity of the projectile orbit makes their individual radiants collapse to merely the same position. Color coding according to the intrinsic collision probability as in the left panel. Bottom panel: The formal collision probability  $p_{\text{Weth}}$  ( $a, e, i; a_0, e_0$ ) during a secular (Lidov–Kozai) cycle shown in the top and left panel (black solid line; the abscissa is time in ky and the ordinate is the intrinsic collision probability in  $\text{AU}^{-2} \text{y}^{-1}$ ). The Lidov–Kozai cycle averaged intrinsic collision probability from our method  $p_{\text{fin}}$  (Eq. (28)) is the blue line, the Wetherill's method based average intrinsic collision probability  $p_{\text{eff}}$  (Eq. (29)) is the green line. (For interpretation of the references to color in this figure legend, the reader is referred to the web version of this article.)

imply an impact on the target, with the limiting configuration given by  $d_{\min} = \tau$ , or

$$\frac{\tau}{a} = \rho = [\eta^2 - \alpha(1 \pm k)]A, \quad (22)$$

with

$$A = \sqrt{\frac{\eta^2 - c^2}{(1 + \beta^2)(\eta^2 - c^2)(1 \pm k)^2 + [h\eta \pm \beta c(1 \pm k)]^2}}. \quad (23)$$

Here we used the Kozai integral  $c = \eta \cos i$  to eliminate the inclination dependence, and replaced the eccentricity  $e$  and argument of pericenter  $\omega$  with the non-singular  $(k, h)$  elements. We now seek the  $(k, h)$  values which simultaneously satisfy Eqs. (22), (23), and (16), or in other words those segments on the  $C$ -integral of orbital secular evolution that provide minimum orbital distances  $d_{\min}$  smaller than the physical size  $\tau$  of the target. In general, there is a number of such discontinuous segments each near the exact crossing condition (18) with (16). The system of algebraic Eqs. (22), (23) and (16) is too complex to allow an analytic solution. We thus developed a simplified linearization method near the exact crossing to solve them (for details see Vokrouhlický et al. (2012) Section 3.2). Each of such segments is crossed in time  $\Delta t$  over the secular cycle of duration  $T_{\text{Kozai}}$ , such that the partial probability  $\Pi_1$  of impact is given by relative duration of this window:  $\Pi_1 = \Delta t / T_{\text{Kozai}}$ . Summing up over all exact intersection configurations, each characterized by  $(e_\star, i_\star, \omega_\star)$  orbital elements of the projectile, we finally have

$$\Pi(r_0) = \sum \left( \frac{\Delta t(r_0)}{T_{\text{Kozai}}} \right)_\star \Pi_2(a, e_\star, i_\star, \omega_\star; r_0). \quad (24)$$

Here we used the principle of uncorrelated partial probabilities  $\Pi_1$  and  $\Pi_2$  discussed above. The final expression for the collision probability per unit of time is given by division by the orbital period  $T_{\text{orb}}$  of the projectile, thus

$$p(r_0) = \frac{\Pi(r_0)}{T_{\text{orb}} \tau^2} = \frac{\mu^{1/2}}{2\pi a^{3/2} \tau^2} \Pi(r_0), \quad (25)$$

where  $\mu = GM$ ,  $G$  is the gravitational constant and  $M$  the mass of the center (the Sun). Note  $p(r_0)$  has been also normalized to the cross-sectional factor  $\tau^2$  of the target, such that it expresses the intrinsic collisional probability (see Öpik, 1951; Wetherill, 1967; Greenberg, 1982). Convenient units of  $p(r_0)$  are  $\text{AU}^{-2} \text{y}^{-1}$ .

#### 2.4. Evaluating collision probability: weighted composition of all possible heliocentric distances of the target

In the previous Section we determined the projectile-target collision probability for a particular heliocentric distance  $r_0$  of the target. In order to evaluate the final collision probability  $p_{\text{fin}}$ , we need to consider all possible values of the distance  $r_0$  in the range  $(r_1, r_2)$ . This basically requires assembling  $p(r_0)$  from Eq. (25) with an appropriate weighting, which should express an uniform circulation of the longitude of pericenter of the projectile's orbit.<sup>3</sup> Observing that the true anomaly differential  $df$  of an elliptic orbit satisfies  $df \propto dr_0 / (r_0^2 |\mathbf{v} \cdot \mathbf{e}_r|) \propto dr_0 / (r_0^2 R_+)$ , we identify the necessary weighting factor to be

$$\Psi(r_0) = \frac{a_0 \eta_0}{\pi} \frac{1}{r_0 \sqrt{(r_0 - r_1)(r_2 - r_0)}}. \quad (26)$$

The explicit value of the constant in the right hand side of Eq. (26) implies the normalization

$$\int_{r_1}^{r_2} \Psi(r_0) dr_0 = 1. \quad (27)$$

Henceforth, we obtain the final intrinsic collision probability  $p_{\text{fin}}$  over all possible impact configurations as

$$p_{\text{fin}} = \int_{r_1}^{r_2} \Psi(r_0) p(r_0) dr_0. \quad (28)$$

Note that the weighting factor  $\Psi(r_0)$  is singular at pericenter and apocenter distances, lower and upper integration bounds in Eq. (28). While finite, numerical evaluation of  $p_{\text{fin}}$  requires some care. Standard methods of integrable singularity removal are briefly recalled in the A.

### 3. Testing the new approach: A comparison with Wetherill's theory and results of the $N$ -body simulations

In this Section we test our approach against results from  $N$ -body simulations and perform comparison with predictions of the Wetherill's method (Wetherill, 1967). Both now allow an eccentric orbit of the target, but the latter assumes the eccentricity and the inclination of the projectile orbit are secularly constant, often violated. On the other hand, our approach still assumes the orbit of the target fixed in the inertial space, a drawback which is to be eliminated in the future work. We expect that at least for targets on low-inclination orbits with respect to the local Laplacian plane our results should be meaningful. It is mainly the effects of projectile's high-inclinations and eccentricities which are tested here.

The projectile's orbit approximately follows a trajectory described by a  $C$ -isolevel of a function in the left hand side of Eq. (16) in the  $(k, h)$  parameter space (see Section 2.2). As recalled by Vokrouhlický et al. (2012), the intersection conditions with a circular orbit of a certain radius  $r_0$ , or simply at a given heliocentric distance  $r_0$ , is geometrically given by the intersection of this trajectory with two displaced circles given by Eq. (18) for both ascending and descending node impacts. For a circular orbit of the target,  $r_0$  was fixed, and we had exquisitely four or eight intersection configurations (except for singular grazing cases). Now the situation is more complicated, because the eccentricity of the target's orbit makes  $r_0$  change during its orbital and secular cycles, and the radii of the circles by which this is represented in the  $(k, h)$  space pulsate (as well as their centers shift). So for a given pair target-projectile we may have the whole set of zero, four and eight intersections over their secular evolution cycle. Obviously, mathematically this is all built in the formulation in Sections 2.3 and 2.4, namely properties of the collision probability  $p(r_0)$  from Eq. (25) and the integration in Eq. (28).

A comparison with Wetherill's approach is not a priori given, but we follow the approach in Vokrouhlický et al. (2012). This is based on what in practical terms one would do without having available our theory. Denote, as above in Eq. (24),  $(e_\star, i_\star, \omega_\star)$  orbital eccentricity, inclination and argument of pericenter that the projectile's orbit acquires during its secular evolution. Adding the quasi-constant semimajor axis  $a$  of the projectile's orbit, and the parameters  $a_0$  and  $e_0$  of the target's orbit, one can formally determine collision probability  $p_{\text{Weth}}(a, e_\star, i_\star; a_0, e_0)$  as if the orbits would satisfy assumptions of the Wetherill's theory. Performing then an average over the projectile's secular cycle of length  $T_{\text{Kozai}}$ , thus

$$p_{\text{eff}} = \frac{1}{T_{\text{Kozai}}} \int_0^{T_{\text{Kozai}}} p_{\text{Weth}}(a, e_\star, i_\star; a_0, e_0) dt, \quad (29)$$

one obtains a proxy for the estimated, long-term collision probability between the projectile and the target. However,  $p_{\text{eff}}$  may not be equal to our value  $p_{\text{fin}}$  from Eq. (28). In fact, it is the degree of their difference that interests us in our tests.

<sup>3</sup> See also discussion in Wetherill (1967) and Greenberg (1982). Note that the apparently expected weighting factor  $dt \propto dr_0 / |\mathbf{v} \cdot \mathbf{e}_r|$ , expressing how much time the projectile spends in the interval  $(r_0, r_0 + dr_0)$ , is already contained in the  $\Pi_2$  probability.

### 3.1. Simple validation of our approach

We first validate our new approach using the simplest possible setup, namely considering a target body and a single projectile. For sake of definiteness the target is on a Mercury-like orbit with  $a_0 = 0.3871$  AU and  $e_0 = 0.2056$ . To make the situation as close as possible to the assumptions of our theory, we assume a single perturbing planet, a Jupiter on a circular orbit at 5.2 AU heliocentric distance. The heliocentric orbital planes of the target body and Jupiter are identical, and both Jupiter and the Sun are given their true masses. We neglect mass of the target body in this section.

In the initial run we took the projectile orbit having the semi-major axis  $a = 0.4$  AU, eccentricity 0.02, inclination  $3^\circ$  and argument of pericenter  $0^\circ$ , implying  $c = 0.99843$  and  $C = 3.98436$ . Such a low-eccentricity and low-inclination orbit will undergo only very limited variations due to Jupiter's perturbation, whose major effect will be near steady circulation of the orbital pericenter and node. Indeed, as shown in the upper left panel of Fig. 1 the secular track of the projectile orbit in the  $(k, h)$  plane is basically a small circle around the center. The simple secular evolution makes the Wetherill's approach fully applicable and we expect a good correspondence between our results and those based on Wetherill's theory. Fig. 1 confirms this conclusion since  $p_{\text{fin}} \approx p_{\text{eff}}$  (bottom panel). Their  $\approx 0.01\%$  difference basically reflects the numerical accuracy with which we evaluate both quantities (less so the very small variations of orbital eccentricity and inclination of the projectile's orbit).

Next, we test a configuration where the orbit of the projectile undergoes one of the possible evolutionary regimes described by the Lidov–Kozai theory. In particular, we set the semimajor axis  $a = 0.9$  AU. We then consider an orbit with starting eccentricity  $e = 0.1$ , inclination  $i = 55^\circ$  and argument of pericenter  $\omega = 0^\circ$ , altogether implying  $c = 0.5707$  and  $C = 0.07446$  constants. Since  $c < \sqrt{0.6}$ , the secular evolution of the projectile's orbit is characterized by large oscillations of both  $e$  and  $i$  as seen on the left top panel of Fig. 2. In this case the argument of pericenter circulates about the origin. A more extreme situation occurs for  $e = 0.6$ ,  $i = 55^\circ$  and  $\omega = 70^\circ$  choice with  $c = 0.45886$  and  $C = -2.80648$ , our second choice of the initial orbit of the projectile. The secular evolutionary track of this orbit is shown in the left top panel of Fig. 3. Here the argument of pericenter oscillates in a limited interval of values about  $90^\circ$  which defines a possible stationary point of the Lidov–Kozai model.

Returning to the first choice of the initial orbit for the projectile, we now focus on Fig. 2. The left top panel shows, apart from the secular track of the projectile's orbit (black curve), also intersection conditions defined by Eq. (18) for all possible values of  $r_0$  in between the pericenter and apocenter of the target's orbit. Each of them is a gray circle, which altogether merge into a 2-D gray area. Unlike in the case of a circular target's orbit, where we have only maximum of 8 intersection configurations, here we formally have an infinite number of them. This is because  $r_0$  ranges a finite interval of values and for each of them we have up to 8 intersections. Some correspond to the grazing configurations for which 8 intersections degenerate to only 4. However, as also discussed by Vokrouhlický et al. (2012), these situations are characterized by a formally large impact probability. This is shown by the color-coded symbols at the top panels of Fig. 2. The top right panel shows location of impact radiants as seen by an observer on the target body (zero longitude fixed at local apex direction). Again, while only a finite number of 8 radiants exist for a circular orbit of the target, we now have an infinity of possibilities (shown by the black rings). Some of them, however, have higher impact probability since they correspond to the grazing configurations of the target-impactor orbits and those are marked by red and yellow symbols. Finally, the bottom panel shows  $p_{\text{Weth}}(t)$  during one Lidov–Kozai cycle

spanning little more than 250 ky (black symbols). These values are computed by Wetherill's approach, assigning formally projectile's orbital elements  $(a, e, i)$  acquired during the orbital evolution along the trajectory shown on the top left panel. These values are sometimes zero for the cases when  $e$  drops below a critical limit such that the pericenter of the projectile's orbit is above the apocenter of the target's orbit and no intersection configurations exist. The Lidov–Kozai averaged collision probabilities defined by Eqs. (28) and (29) are  $p_{\text{fin}} \approx 2.58 \text{ AU}^{-2} \text{ y}^{-1}$  and  $p_{\text{eff}} \approx 2.16 \text{ AU}^{-2} \text{ y}^{-1}$ , showing only a minor difference in this situation. This is because even in the Lidov–Kozai regime the impacts are possible only over a limited interval of secular evolution cycle, during which eccentricity and inclination values do not change significantly (Fig. 2). A larger difference of the two approaches is exhibited by the apparent impact radiants in the top right panel. The red dots correspond formally to those obtained by Wetherill's theory, the same way as  $p_{\text{Weth}}(t)$  is computed. These apparent, but fake, radiants span a quite larger region on the local sky of the observer moving together with the target than the true radiants shown by the black loops.

Fig. 3 shows the similar data for the second chosen initial orbit of the projectile. In this case, the orbital argument of pericenter  $\omega$  oscillates about the  $90^\circ$  stationary point of the Lidov–Kozai model, so apparently assumptions of the Wetherill's approach are strongly violated. The three panels show again evolution of the projectile orbit and intersection conditions in the  $(k, h)$  plane, radiant locations with respect to the apex system of the target and  $p_{\text{Weth}}(t)$  during one Lidov–Kozai cycle. The restricted evolution  $\omega$  makes now only two radiant locations appear, though formally there is again a continuum of possible radiants distributed along the loop-like region. The averaged collision probabilities are  $p_{\text{fin}} \approx 6.54 \text{ AU}^{-2} \text{ y}^{-1}$  and  $p_{\text{eff}} \approx 5.72 \text{ AU}^{-2} \text{ y}^{-1}$ . Again, their difference is not large, essentially reflecting only small variations of eccentricity and inclination values for impact configurations.

### 3.2. Comparison with $N$ -body simulations

We further validate conclusions from the previous Section by performing a comparison between the expected number of impacts, based on the collision probability calculation, and their direct record performed by numerical integration. We keep the setup described above, namely considering the Sun and Jupiter as massive bodies and a massless target on a Mercury-like orbit, coplanar with that of Jupiter. In order to accelerate the impact rate in our simple experiment, we assumed the target has ten times larger radius than Mercury (i.e.,  $\tau \approx 1.63 \times 10^{-4}$  AU). We considered two sets of projectiles, each consisting of 500 test particles. Instead of starting them from very nearby orbits, we distributed them evenly during the Lidov–Kozai secular cycle of orbits shown in Figs. 2 and 3 (top left panels). The initial data were actually created with the help of integration described in Section 3.1, making an output of orbital elements  $(e, i, \omega)$  (recall  $a = 0.9$  AU is secularly constant). All integrations were performed using the `SWIFT_RMVS3` package,<sup>4</sup> that is able to record direct impacts onto the target. We used 0.5 day integration timestep to resolve fast motion of the Mercury-like target planet.

In our simplified model there are no other sinks of test particles other than the impact on the target. Since the impacts are probabilistic, Poisson process, we have a simple estimator of the cumulative impactor time profile:  $N_{\text{imp}}(t) = N_0 [1 - \exp(-t/T)]$  ( $N_0 = 500$  in our case). Here,  $T$  is a characteristic timescale, given by  $T = 1/(\tau^2 p)$ , where  $p$  is the collision probability. We have three alternative formulations of  $p$ , namely  $p_{\text{fin}}$  from our theory,  $p_{\text{eff}}$  from the formal application of the Wetherill's theory and also we introduce

<sup>4</sup> <http://www.boulder.swri.edu/~hal/swift.html> (Levison and Duncan, 1994).

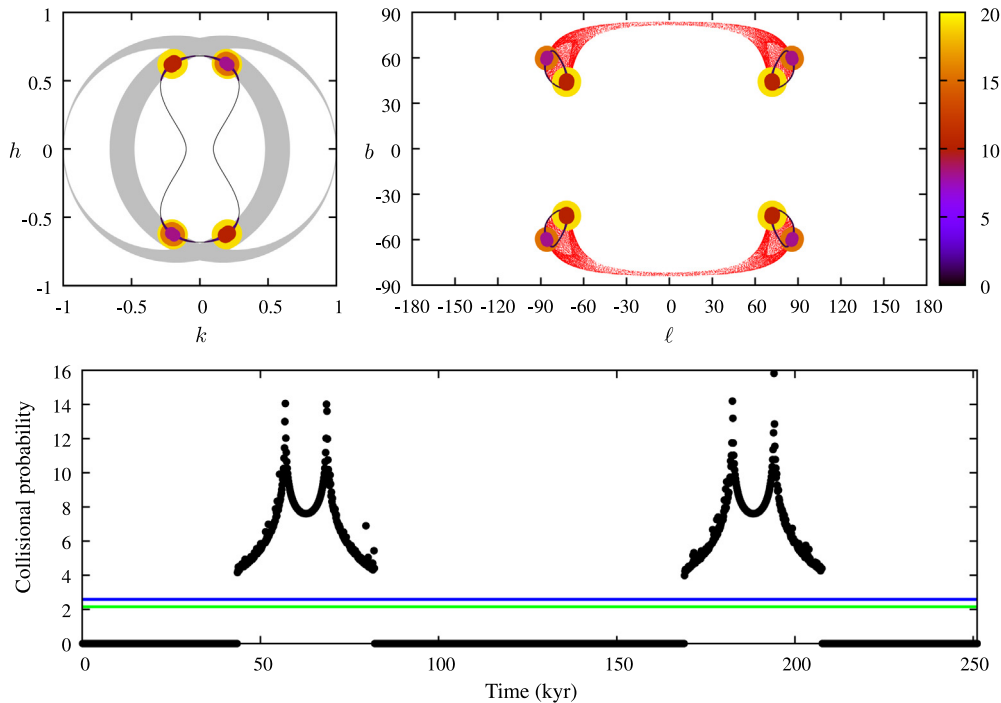


**Fig. 2.** The same as Fig. 1, but now for the projectile with the semimajor axis  $a = 0.9$  AU, the initial eccentricity  $e = 0.1$ , inclination  $i = 55^\circ$  and argument of pericenter  $\omega = 0^\circ$ . Top and left: The evolution trajectory during one secular, Lidov–Kozai cycle (black line), defined by the  $\mathcal{P}(k, h; c) = C$  integral from Eq. (16)), is now different from a simple circle. Exact impact condition with the target body is graphically shown by the set of gray circles (both ascending and descending nodes) and they correspond to solutions of Eq. (18) for all possible target heliocentric distances  $r_0$ . Impacts are possible only in the region of black line crossing with gray circles. The color coding corresponds to the individual values of collision probability  $p(r_0)$  (see also the bar on the right). Maxima are for the pericentric configurations. Top and right: Radiant position in the apex coordinate system – larger eccentricity of the projectile orbits makes the radiants span four loop-like regions on the local sky of the target-based observer. The set of red dots are fake radiants formally constructed by Wetherill's approach and combinations of  $(a, e, i, \omega)$  orbital elements of the projectile and  $(a_0, e_0)$  orbital elements of the target. Bottom panel: The formal collision probability  $p_{\text{Weth}}(a, e, i, \omega; a_0, e_0)$  during a secular (Lidov–Kozai) cycle shown in the top and left panel (black solid line). Zero values for no crossing conditions between the projectile and target orbits. The Lidov–Kozai cycle averaged intrinsic collision probability from our method  $p_{\text{fin}}$  (Eq. (28)) is the blue line, the Wetherill's method based average intrinsic collision probability  $p_{\text{eff}}$  (Eq. (29)) is the green line. (For interpretation of the references to color in this figure legend, the reader is referred to the web version of this article.)

$p_{\text{circ}}$  for the circular orbit of the target based on Vokrouhlický et al. (2012), so that we can compare the three estimators of the decay timescale  $T_{\text{P\&V}} = 1/(\tau^2 p_{\text{fin}})$ ,  $T_{\text{Weth}} = 1/(\tau^2 p_{\text{eff}})$  and  $T_{\text{VPN}} = 1/(\tau^2 p_{\text{circ}})$  with the numerically determined value, where  $p_{\text{circ}}$  is computed formally as if the target had semimajor axis  $a_0$  and zero eccentricity.

Fig. 4 shows results for projectiles on orbits similar to that of Fig. 2. Our estimated decay timescale is  $T_{\text{P\&V}} \simeq 14.63$  Myr and  $T_{\text{Weth}} \simeq 17.63$  Myr. In case of the circular target there are no possible impacts, thus  $T_{\text{VPN}}$  is formally infinite since  $p_{\text{circ}} = 0$ . The corresponding  $N_{\text{imp}}(t)$  profiles (gray curves) are shown on the left panel and compared with the recorded sequence of impacts (dark symbols). An eye-based comparison would favor results from our recent theory. Indeed, fitting the real impact record with the  $N_{\text{imp}}(t)$  law would yield  $T_{\text{Fit}} = 15.46 \pm 0.03$  Myr. Additional support for our conclusions comes from comparison of the predicted impactor radiants and those determined from the numerical simulation. This is shown on the right panel of Fig. 4. Our predicted loop-like radiant distribution is indeed very well matched by the location of numerically recorded radiants (black symbols).

Fig. 5 shows the same for projectiles on orbits similar to that of Fig. 3. Since the collision probabilities were larger now, the decay time constant is shorter and the population fades faster. We obtain  $T_{\text{P\&V}} \simeq 5.79$  Myr,  $T_{\text{Weth}} \simeq 6.62$  Myr and  $T_{\text{VPN}} = 2.64$  Myr, while the fit to numerically-determined  $N_{\text{imp}}(t)$  provides  $T_{\text{Fit}} = 5.65 \pm 0.01$  Myr. Again, the radiant distribution shown on the right panel of Fig. 5 indicates an excellent correspondence between the theory prediction and the numerically recorded impacts. Both situations

provide a good illustration of differences between new and previous formalisms.

#### 4. A real life application: Impactors from the E-belt

The examples discussed in the previous Section indicated validity of our results, as well as their numerical implementation in our code, but what does it say about their “real-life” applicability. After all, these cases were highly simplified: we used only one disturbing planet in a fixed elliptic orbit, a coplanar massless target, which implied that the particles (projectiles) conserved their initial Lidov–Kozai integrals  $c$  and  $C$ . In reality, though, the situation is different. All planets are massive and interacting, which complicates the secular evolution of the projectile orbits. Moreover, as the projectile interact with the planets in a short-range close approaches, their orbital semimajor axis is not conserved. Some may be brought close to mean motion resonances with the target orbit. All these effects invalidate, strictly speaking, assumptions of both Wetherill's and ours approaches. Still, we may be interested to know how they perform in such a complex case.

Our “real-life case” is based on the recent work of Bottke et al. (2012) who examined a decay of a putative past extension of the main asteroid belt toward smaller heliocentric distances, bounded basically by the outermost terrestrial planet. Bottke et al. (2012) called this extension the E-belt and found several intriguing facts in favor of this population out of which we mention two outstanding: (i) the E-belt is a natural source of projectiles that impacted terrestrial planets and the Moon during the Archaean period and

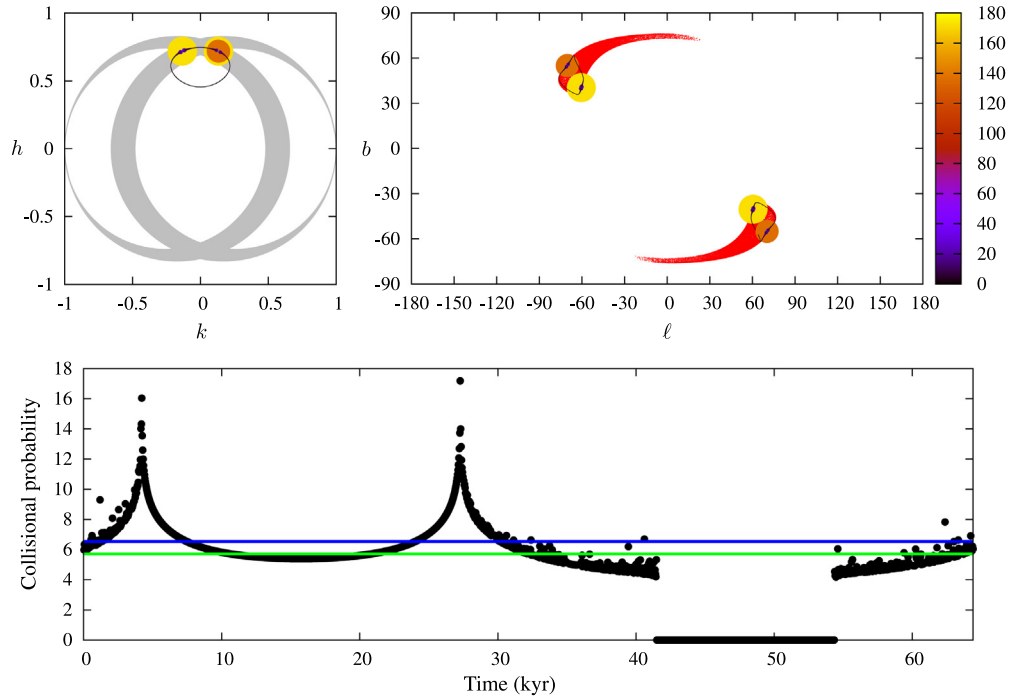


**Fig. 3.** The same as in Fig. 2, but now for the projectile's orbit with semimajor axis  $a = 0.9$  AU, initial eccentricity  $e = 0.6$ , inclination  $i = 55^\circ$  and argument of pericenter  $\omega = 70^\circ$ . Top and left: The argument of pericenter  $\omega$  now circulates about the stationary solution offset from the center in the  $(k, h)$  plane and thus acquires values from a limited interval of values around  $90^\circ$ . Top and right: Absence of  $\omega$  values near  $180^\circ$  makes number of radiant locations reduced to two, loop-like structures. Bottom panel: The behavior of the secular-evolution trajectory, black line on the top and left panel, makes the Lidov–Kozai cycle be effectively half of that seen on Fig. 2. Hence, the  $p_{\text{Weth}}(a, e_*, i_*; a_0, e_0)$  values resemble those from the first part of the bottom panel on Fig. 2. Systematically higher eccentricity  $e_*$  offers more chance for the impact configurations, and thus the  $p_{\text{Weth}}(a, e_*, i_*; a_0, e_0) = 0$  interval is shorter. Consequently, also the values  $p_{\text{Weth}}$  and  $p_{\text{eff}}$  are larger.

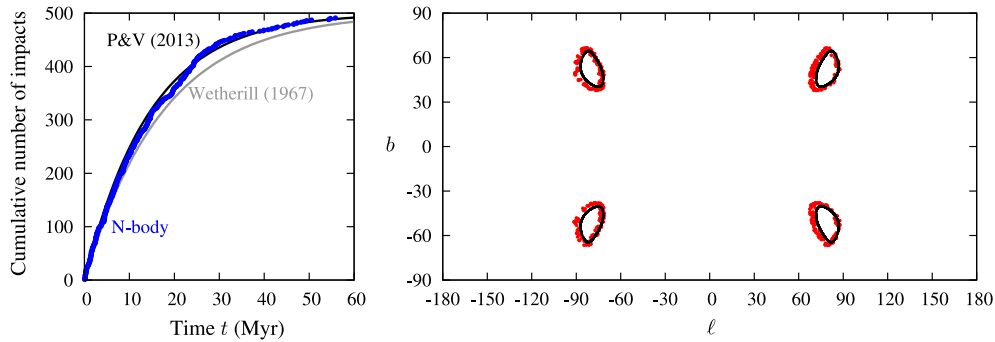


**Fig. 4.** Impact conditions for a population of  $N_0 = 500$  test particles distributed evenly along the secular-cycle trajectory shown by the black line on the top and left panel of Fig. 2. Massless target body on a Mercury-like orbit with  $a_0 = 0.3871$  AU and  $e_0 = 0.2056$ , and radius  $\tau \simeq 1.63 \times 10^4$  AU (about ten times larger than that of Mercury). A single, Jupiter-like planet feeds the secular evolution of the projectile population. Left: Cumulative number of impacts onto the target body as a function of time  $t$  since the beginning of the numerical simulation. Blue symbols directly from the numerical run, while the black and gray lines are estimators from the collision impact approaches developed here and the Wetherill's method, i.e.,  $N_{\text{imp}}(t) = N_0 [1 - \exp(-t/T)]$  with some  $T$  timescale. Our method gives  $T_{\text{P\&V}} = 14.63$  Myr, Wetherill's approach yields  $T_{\text{Weth}} = 17.43$  Myr. In absence of other sinks all projectiles eventually hit the target. For the circular orbit of the target, there are no possible impact configurations. Right: Comparison of radiant position as recorded directly from the numerical simulation (red symbols) and predicted from our approach (black lines, see also top and left panel on Fig. 2). The abscissa is the longitude measured from the apex direction as seen by an observer on the target body, the ordinate is latitude in the same system (both in degrees). (For interpretation of the references to color in this figure legend, the reader is referred to the web version of this article.)

dominantly contributed to what is known as the Late Heavy Bombardment (LHB), and (ii) the E-belt provides a natural source of to-days small population of Hungaria asteroids.

Similarly to Bottke et al. (2012) we thus considered a population of particles initially located in the E-belt and numerically integrated the post-LHB evolutionary phase. This means planets are assumed to have acquired their current orbits. On the contrary to the work of Bottke et al. (2012), where planet Mercury was neglected, we include it in our current simulation. We thus need to use a considerably shorter integration timestep of 0.5 days. On the other hand, the purpose of our simulation is rather illustrative,

so we do not need to develop the model in such a detail as Bottke et al. (2012). For instance, we omit the pre-LHB evolution of the E-belt objects. Luckily, Bottke et al. (2012) have shown that this phase has only limited effects on both number of objects and their orbital distribution in the E-belt. So our starting orbits of the E-belt particles had a uniform distribution of semimajor axes between 1.7 AU and 2.1 AU, eccentricities  $e$  and inclinations  $i$  distributed using a Maxwellian distribution with the peak values of 0.15, and  $8.5^\circ$  respectively, and the standard deviation values of 0.07, and  $7^\circ$  respectively. We eliminated bodies that would initially cross the orbit of Mars, an expected result of the pre-LHB orbital

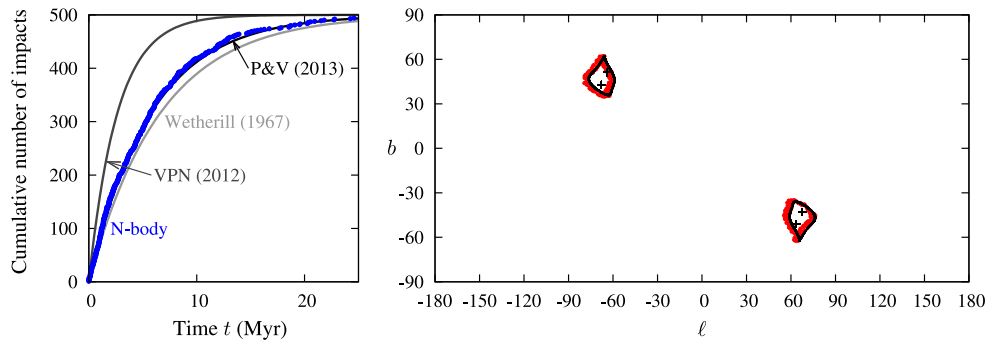


**Fig. 5.** The same as in Fig. 4 but for a population of particles distributed evenly along the secular-cycle trajectory shown by the black line on the top and left panel of Fig. 3. Left: Because of the larger  $p_{\text{fin}}$  and  $p_{\text{eff}}$  values, the characteristic timescale of projectile elimination is shorter now:  $T_{\text{P&V}} = 5.79$  Myr and  $T_{\text{Weth}} = 6.62$  Myr. While both are similar, our value slightly better expresses the real track of the impacts (blue symbols). The formal result for the theory where the orbit of the target is circular is represented by dark-gray line with the characteristic timescale  $T_{\text{P&V}} = 2.64$  Myr. In this case it represents the worst estimate of the impact dynamics. Right: As expected, radiants of impacting particles are now fewer and located in only two quadrants on the sky. Directly recorded radiants (red symbols) correspond to their predicted locations (black loops) quite well. The limited number of 4 impact configurations for the circular orbit of the target (dark-gray crosses) cannot express the exact structure of recorded radiants, however it can provide approximate their position. (For interpretation of the references to color in this figure legend, the reader is referred to the web version of this article.)

evolution. Longitudes of node and pericenter, as well as the mean anomaly, were distributed randomly between  $0^\circ$  and  $360^\circ$ . Altogether we started 5000 E-belt particles. Initial values of osculating ( $a, e, i$ ) are shown on the leftmost panel of Fig. 6. All planets were given their masses and initial orbits as of J2000.0 epoch. In order to speed up the simulation, we multiplied planetary radii by a factor 5, increasing thus their geometric cross-section by a factor 25. We used `SWIFT_RMVS3` package to propagate orbits of planets and particles for 500 Myr and recorded their fate. Few particles survived in heliocentric motion, while majority reached some of the possible end-states: either impacted one of the planets or the Sun, or was pushed onto Jupiter-crossing orbits and was ejected from the Solar System. We output state vectors of all bodies every

100 years, providing us a clue about their orbital evolution. In order to resolve orbital behavior near the Sun, and thus not to miss possible Mercury impacts, we set the minimum heliocentric distance 0.01 AU, about two solar radii. While some projectiles may survive even closer approaches to the Sun, many would tidally or thermally disintegrate.

Thanks to the increased planetary radii in our numerical experiment we have recorded enough impacts onto terrestrial planets directly from the numerical simulation. This information is considered as a ground truth, which is to be compared with predictions from either of the two approaches discussed above. This is to be done as follows. The projectile population  $N(t)$  decays with time  $t$  according to

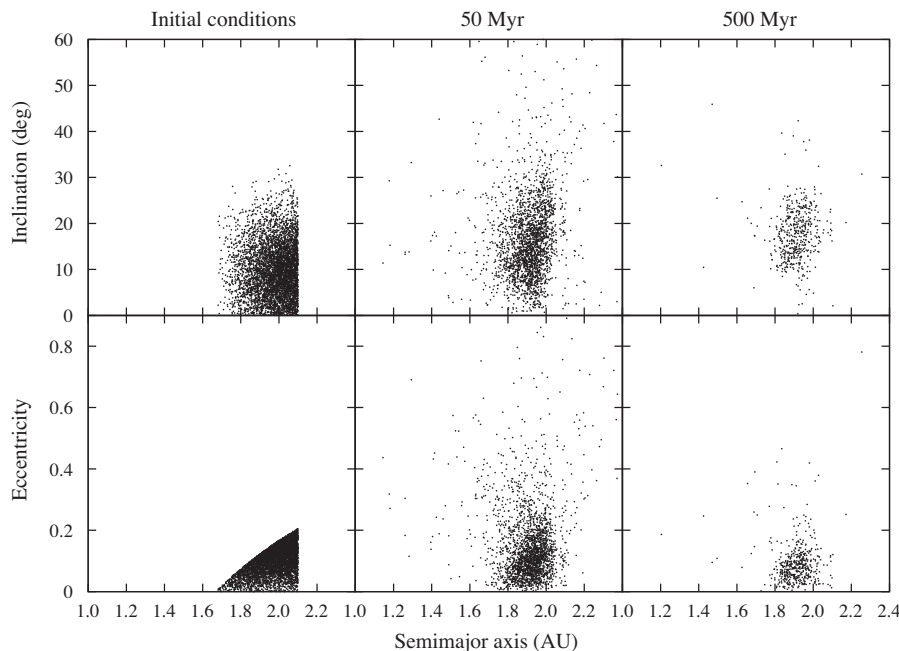


**Fig. 6.** Post LHB dispersal of the E-belt population. Upper panels show semimajor axis vs inclination, bottom panels show semimajor axis vs eccentricity of the numerically propagated orbits. Left: Initial data of 5000 particles in our simulation. Semimajor axis was distributed uniformly in between 1.6 AU and 2.1 AU. Eccentricity and inclinations had Maxwellian distribution with maxima at 0.15 and  $8.5^\circ$ , and standard deviation of 0.07 and  $7^\circ$ , respectively. All particles having initially Mars-crossing orbits were eliminated (bottom panel). Middle: Population at 50 Myr. Planetary perturbations make the population dispersed. Because of the predominant high inclinations and low eccentricities the characteristic decay timescale is long. At this moment still 46% of particles survive. The remaining were eliminated by several possible orbital end-states: impact on the Sun or the planets, or ejection from the Solar System. Right: Population at 500 Myr has seen depletion at lower inclinations and higher eccentricities (some 10% particles still survived). The surviving orbits converge to what is today observed as the Hungaria population.

**Table 1**

A summary of cumulative number of impacts on terrestrial planets at the end of simulation,  $T = 500$  Myr, obtained by different methods: (i)  $N_{\text{direct}}$  denotes number of direct impacts recorded by SWIFT code, (ii)  $N_{\text{PV}}$  is a cumulative number of impacts based on evaluation of intrinsic collisional probability at each time step using our theory (Eq. (31)), (iii)  $N_{\text{Weth}}$  is the same as  $N_{\text{PV}}$  but using Wetherill's theory, and (iv)  $N_{\text{VPN}}$  is the same as  $N_{\text{PV}}$  but using only the circular orbit of the target.

Planet	$N_{\text{direct}}$	$N_{\text{PV}}$	$N_{\text{Weth}}$	$N_{\text{VPN}}$
Mercury	64	58.03	43.65	55.82
Venus	491	491.04	493.09	482.03
Earth	765	808.78	826.69	787.77
Mars	818	884.88	547.99	793.28

$$dN = -(P_{\text{tot}} + P')dt. \quad (30)$$

Here  $P_{\text{tot}}(t) = \sum_i \bar{p}_{\text{fin}}^i(t) \tau_i^2$  is the estimate of the composite probability per unit of time to impact one of the terrestrial planets (hence the summation index goes from 1 to 4 spanning Mercury to Mars). The total intrinsic collision probability with respect to the specific target planet  $\bar{p}_{\text{fin}}^i(t)$  is itself given as a population sum over the projectiles, i.e.  $\bar{p}_{\text{fin}}^i(t) = \sum_{j=1}^{N(t)} p_{\text{fin}j}^i$ , where the summation here goes over all projectile particles. Their individual intrinsic collision probabilities  $p_{\text{fin}j}^i$  with the target planet  $i$  are computed by using Eq. (28) with their current osculating orbital elements  $(a, e, i, \omega)$ . Obviously, due to a more complex long-term orbital evolution of the particles than described in Section 2.2 this is only an approximation. Moreover, the right hand side of Eq. (30) contains also a second part of the probability for particle elimination, namely  $P'$ . This is because in our simulation there are now more sinks than impacts on terrestrial planets. First, there is a possibility to impact the Sun, but also some orbits may be pushed to larger heliocentric distance, impact giant planets or be ejected from the Solar System. All these processes are collectively described by  $P'$ . However, since we do not dispose with an appropriate formulation of  $P'$ , we do not solve the Eq. (30), rather we take its solution  $N(t)$  as directly given by the SWIFT propagation. Still, we can estimate cumulative number of planetary impacts until time  $T$  using (for the  $i$ th planet).

$$N_{\text{PV}}^i(T) = \int_0^T dt \tau_i^2 \bar{p}_{\text{fin}}^i(t), \quad (31)$$

and similarly  $N_{\text{Weth}}^i(T)$  by replacing  $\bar{p}_{\text{fin}}^i(t)$  with Wetherill's direct estimator  $\bar{p}_{\text{Weth}}^i = \sum_{j=1}^{N(t)} p_{\text{Weth}j}^i$ , and  $N_{\text{VPN}}^i(T)$  for the circular orbit of the target with  $\bar{p}_{\text{circ}}^i(t)$ .

Fig. 6 shows snapshots of the projectile osculating orbits at epochs 0 Myr, 50 Myr and 500 Myr. As expected from Bottke et al. (2012), the E-belt particles are swiftly dispersed with longest lived ones pushed on low-eccentricity orbits with high inclination. Eventually, a tiny residual of such a population survives till now as Hungaria asteroids. In course of Gys though, the remaining part of the E-belt was eliminated. For instance, at 50 Myr (middle panel of Fig. 6) only 46% of particles survived, and at 500 Myr (right panel of Fig. 6) only 10% of particles survived. Most of the eliminated particles impact the Sun, as typical for terrestrial planet crossing orbits, but some hit the planets. Fig. 7 shows the cumulative record of planetary impacts as obtained from our numerical experiment (symbols). We also show the computed functions  $N_{\text{PV}}^i(T)$  for our theory (green line),  $N_{\text{Weth}}^i(T)$  for Wetherill's theory (red line) and  $N_{\text{circ}}^i(T)$  for circular orbit of the target (blue line), and make them compared with the true impacts. In spite of minor drawbacks both  $N_{\text{PV}}^i(T)$  and  $N_{\text{VPN}}^i(T)$  match the real impacts better than  $N_{\text{Weth}}^i(T)$ , especially for Mercury and Mars. Earth and Venus impact record is equally well reproduced by  $N_{\text{PV}}^i(T)$ ,  $N_{\text{VPN}}^i(T)$  and  $N_{\text{Weth}}^i(T)$ . The good coincidence between  $N_{\text{PV}}^i(T)$  and  $N_{\text{VPN}}^i(T)$  in the case of these two planets is no surprise because of their very low eccentricity. It is somewhat more surprising that  $N_{\text{VPN}}^i(T)$  still represents well the impact record on Mars and Mercury (in the Mars case even better than  $N_{\text{PV}}^i(T)$ ). This is obviously only formal to a certain degree, because – as we discuss below – the individual particle orbits evolve in a very complicated way which does not satisfy assumptions of any of the approaches. The good performance of the Vokrouhlický et al. (2012) approach is, however, promising, because of much lower CPU requirements than the current theory. A summary of cumulative number of impacts on terrestrial planets at the end of the simulation,  $T = 500$  Myr, obtained by different methods is shown in Table 1.

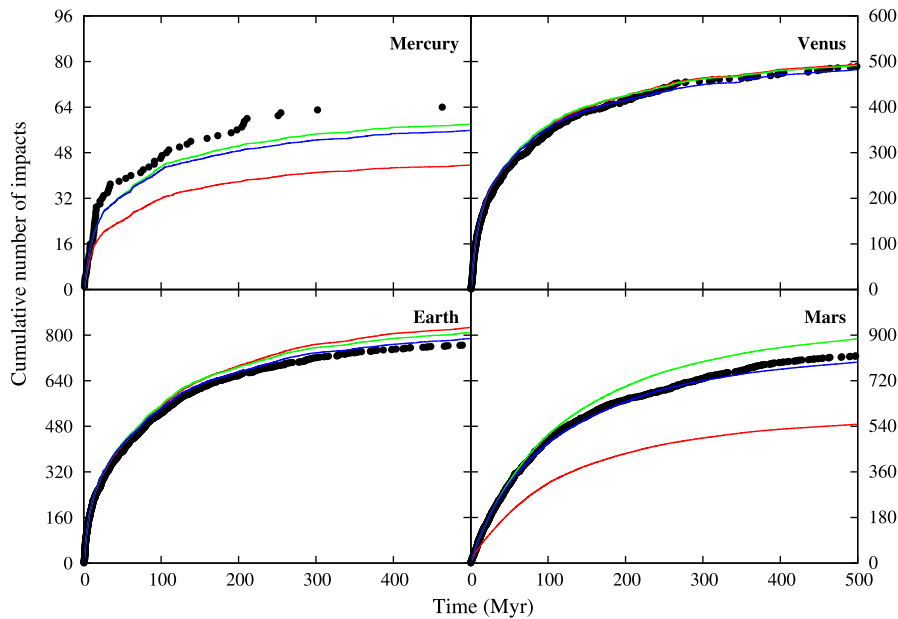


**Fig. 7.** Cumulative number of E-belt particles impacting terrestrial planets. Time origin at the reconfiguration of giant planets (start of the LHB Bottke et al., 2012). Terrestrial planet had their radii multiplied by a factor 5 in our simulation, so the absolute number of impacts is larger than in reality; their ratio – if corrected for small focusing effects – is however correct. Symbols are directly recorded impacts in our numerical simulation. Green line is prediction  $N_{\text{PV}}^i(T)$  from our theory, red line is prediction  $N_{\text{Weth}}^i(T)$  from Wetherill's approach, and blue line is prediction  $N_{\text{VPN}}^i(T)$  for the circular orbit of the targets (see the text). (For interpretation of the references to color in this figure legend, the reader is referred to the web version of this article.)

Interestingly, Mercury and Venus have the majority of E-belt impact events skewed toward earlier epochs after LHB than Earth and especially Mars. In quantitative terms, 50% of Mercury impacts occur within the first 25 Myr, while 50% of Mars impacts extend over 75 Myr after LHB. In total, Earth receives about 12 times more impacts than Mercury. The ratio of geometric cross section of the Earth and Moon is  $\approx 13.5$  and since the post-LHB impact velocities of the E-belt projectiles for Earth are  $\approx 20 \text{ km s}^{-1}$  (Bottke et al., 2012), the focusing factor plays a minor role in increasing flux on the Earth with respect to the Moon. In reality, this factor would have been about 1.5, but in our simulation the Earth radius was increased such that the focusation plays virtually no role. From this we infer that Mercury should obtain about the same number of E-belt impacts as the Moon (maybe only 10–20% more). Obviously, since the impact velocity on Mercury is larger – median value of  $\approx 42 \text{ km s}^{-1}$  (Marchi et al., 2009) – equal size projectile would create somewhat larger craters on Mercury than on the Moon. The exact factor obviously depends on the scaling law used, but it could be  $\approx \sqrt{2}$ . Assuming a collisionally evolved population of impactors, there would be about  $\approx \sqrt{2}^{2.5} \approx 2.5$  more E-belt produced craters of a given size on Mercury than on the Moon. However, if rescaled to the crater density, one has to take into account an about twice larger surface area of the Mercury, the equal-size E-belt produced craters would have only slightly larger density on Mercury than on the Moon.

We find the Mars impact record interesting, since it has the longest-lived tail of the E-belt bombardment. This is in fact understandable, being just next to the E-belt population. We find also interesting that here the formal application of the Wetherill's approach fails, while results from our theory – while not being perfect – match the data better. This is perhaps because the longer-lived orbits keep having high inclination and low eccentricity, such that impacts on Mars are often nearly pericentric. This increases the collision probability. Another planet, where we observe largest difference between prediction from our model and Wetherill's approach is Mercury. Here again, impactors that make it to Mercury's heliocentric distance likely keep having high-orbital inclination, a situation better described by our approach.

## 5. Conclusions

We extended the collision probability theory for the high inclination and high eccentricity projectile orbits presented in our previous paper Vokrouhlický et al. (2012). In particular, our present form can handle the target on an elliptic orbit with uniform precession in space. Generalization to target orbits with non-zero inclination and regular node precession, sweeping thus a final volume in space, is left for future work.

We tested our approach using simple projectile-target configurations, mainly to demonstrate the principal phenomena and to verify performance of our numerical code. We also ran a simplified numerical experiment (planetary radii 5 times inflated) of the E-belt population dispersal after planets acquired their final architecture. A full-fledged planetary system, including planet Mercury was used. This allowed us to compare directly recorded planetary impacts with prediction of our collision theory even for this innermost planet. Surprisingly, even that the orbital evolution of the individual E-belt particles is well beyond (and far more complex) the assumptions about secular evolution in our approach, we note rather fair performance of our theory.

The code providing intrinsic collision probability, position of radiant and impact velocities based on our approach written in FORTRAN 77 language is available at <http://sirrah.troja.mff.cuni.cz/~pokorny/Kozai/>.

## Acknowledgments

This research was supported by the Czech Grant Agency (Grant P209-13-01308S), the Grant Agency of the Charles University (Grant 602213) and the Project SVV-267301 of the Charles University in Prague. We thank the referees, Giovanni F. Gronchi and Gerhard J. Hahn, for suggestions that helped to improve the original version of this paper.

## Appendix A. A comment on numerical evaluation of Eq. (28)

Numerical evaluation of several integrals introduced in Section 2 require specific care. This is because while finite, functions in their integrands may be singular. For instance, the weighting function  $\Psi(r_0)$  in the integrand of Eq. (28) diverges when  $r_0 = r_1$  and  $r_0 = r_2$ , the limits of the integration. Obviously, in this case the situation is simple and a standard parameter transformation helps to remove the singularities (see Press et al., 1992, Chapter 4.4). We first split the integral into two pieces, integrating once from  $r_1$  to  $a_0$  and next from  $a_0$  to  $r_2$ . In the former case we use the following substitution

$$\int_{r_1}^{a_0} \frac{p(r_0) dr_0}{r_0 \sqrt{(r_0 - r_1)(r_2 - r_0)}} = \int_0^{\sqrt{a_0 r_0}} \frac{2p(r_1 + t^2) dt}{(r_1 + t^2) \sqrt{r_2 - r_1 - t^2}}, \quad (\text{A.1})$$

while in the latter case, we have

$$\int_{a_0}^{r_2} \frac{p(r_0) dr_0}{r_0 \sqrt{(r_0 - r_1)(r_2 - r_0)}} = \int_0^{\sqrt{a_0 r_0}} \frac{2p(r_2 - t^2) dt}{(r_2 - t^2) \sqrt{r_2 - r_1 - t^2}}. \quad (\text{A.2})$$

We adopted Romberg's method for evaluation of these definite integrals.

The main difficulty now resides in the a priori unknown and potentially ill-behaved course of a function  $p(r_0)$ , while the rest of the integral is easily evaluated using even a small number of iterations of the Romberg scheme. The potential problems are due to grazing pericentric or apocentric impact configurations for a fixed impactor orbit and varied  $r_0$  value. These situations are typically badly behaved in the linear approximation of the two orbits and result in singularity of apparent  $p(r_0)$  (see, e.g., Appendix of Vokrouhlický et al. (2012)). At this moment, we did not optimize our code to deal in detail with all these caveat. Rather, we adopted a pragmatic deal between efficiency and precision of the code. This may degrade its performance at some singular configurations, but overall provides useful tool for most of the situations.

## References

- Bailey, M.E., Chambers, J.E., Hahn, G., 1992. Origin of sungrazers – A frequent cometary end-state. *Astron. Astrophys.* 257, 315–322.
- Bottke, W.F. et al., 2012. An Archaean heavy bombardment from a destabilized extension of the asteroid belt. *Nature* 485, 78–81.
- Greenberg, R., 1982. Orbital interactions – A new geometrical formalism. *Astron. J.* 87, 184–195.
- Gronchi, G.F., Milani, A., 1998. Averaging on Earth-crossing orbits. *Celest. Mech. Dynam. Astron.* 71, 109–136.
- Gronchi, G.F., Milani, A., 1999. The stable Kozai state for asteroids and comets. With arbitrary semimajor axis and inclination. *Astron. Astrophys.* 341, 928–935.
- Kessler, D.J., 1981. Derivation of the collision probability between orbiting objects. The lifetimes of Jupiter's outer moons. *Icarus* 48, 39–48.
- Kinoshita, H., Nakai, H., 2007. General solution of the Kozai mechanism. *Celest. Mech. Dynam. Astron.* 98, 67–74.
- Kozai, Y., 1962. Secular perturbations of asteroids with high inclination and eccentricity. *Astron. J.* 67, 591–598.
- Levison, H.F., Duncan, M.J., 1994. The long-term dynamical behavior of short-period comets. *Icarus* 108, 18–36.
- Lidov, M.L., 1961. The evolution of orbits of artificial satellites of planets under the action of gravitational perturbations of external bodies. *Artif. Satell. Earth* 8, 5–45.
- Lidov, M.L., 1962. The evolution of orbits of artificial satellites of planets under the action of gravitational perturbations of external bodies. *Planet. Space Sci.* 9, 719–759.

- Marchi, S., Mottola, S., Cremonese, G., Massironi, M., Martellato, E., 2009. A new chronology for the Moon and Mercury. *Astron. J.* 137, 4936–4948.
- Morbidelli, A., 2002. *Modern Celestial Mechanics: Aspects of Solar System Dynamics*. Taylor & Francis, London.
- Öpik, E.J., 1951. Collision probability with the planets and the distribution of planetary matter. *Proc. R. Irish Acad. Sect. A* 54, 165–199.
- Press, W.H., Teukolsky, S.A., Vetterling, W.T., Flannery, B.P., 1992. *Numerical Recipes in FORTRAN, .. The Art of Scientific Computing*, second ed. University Press, Cambridge.
- Thomas, F., Morbidelli, A., 1996. The Kozai resonance in the outer Solar System and the dynamics of long-period comets. *Celest. Mech. Dynam. Astron.* 64, 209–229.
- Vokrouhlický, D., Pokorný, P., Nesvorný, D., 2012. Öpik-type collision probability for high-inclination orbits. *Icarus* 219, 150–160.
- Wetherill, G.W., 1967. Collisions in the asteroid belt. *J. Geophys. Res.* 72, 2429–2444.